AGB Mass-loss Rates and Metal Yields from Scaled Mixing-length and Mass-loss Parameters

Ezra Huscher[1,2⋆], Kristian Finlator[1,2], Jason Jackiewicz[1]

[1] *Department of Astronomy, New Mexico State University, Las Cruces, NM, USA*
[2] *Cosmic Dawn Center (DAWN) Niels Bohr Institute, University of Copenhagen, Denmark*

28 September 2025

ABSTRACT

Stars on the asymptotic giant branch enrich the interstellar medium with carbon, nitrogen, and dust, which in turn boost cooling and promote future generations of planet and star formation. They are poorly-constrained observationally because they remain in this phase briefly and pulsate on long timescales. At the same time, modeling AGB stars is challenging because they undergo rapid mass loss and complex convective mixing and nucleosynthesis. By incorporating updated opacity tables and instability management techniques into MESA, we compute a new grid of AGB models that densely samples a wide range of initial masses ($0.8 \leqslant M_{\odot} \leqslant 7$) and metal mass fractions ($0.0001 \leqslant Z \leqslant 0.03$. We develop scaling formulas for varying the convective mixing length and Blöcker mass loss parameters, enabling calibration against recent carbon star luminosity observations and hydrodynamic simulation results. We provide metal yields of ^{12}C, ^{13}C, ^{13}N, ^{14}N, ^{15}N, ^{16}O, ^{17}O, ^{18}O, ^{19}F, ^{20}Ne, ^{22}Ne, ^{24}Mg and ^{28}Si for galactic chemical evolution models and updated input tables for AGB mass loss rates and metal yields for cosmological simulations. Our new models are consistent with observations of the stellar initial-final mass relation derived from white dwarf progenitor masses, typical AGB mass-loss rates of $\sim 10^{-7}$ to 10^{-5}M$_{\odot}$/year, and average luminosities for AGB populations of carbons stars of $\sim$ 8200L$_{\odot}$. We compare yields to previous models, finding similar C, N, O, F, and Ne but significantly enhanced Mg. The surface C/O ratios match other models at high metallicity but tend to be higher at Z$\leqslant$0.005. Predicted surface metallicities match previous simulation assumptions, but significantly higher AGB outflow rates suggest large systematic uncertainties in the theoretically-expected cosmological carbon yield.

1 INTRODUCTION

1.1 Background

The asymptotic giant branch (AGB) phase of a star's evolution is a brief and lively period *with considerable implications for galaxy evolution and observational astronomy.* There is increasing evidence that AGB stars play a key role in the intrinsic brightness and distinctive spectral features of their host galaxies. They also produce considerable amounts of dust from condensation of their ejected material that impacts everything from star formation to the development of complex chemistry (Gehrz et al. 1989; Li et al. 2019).

All intermediate-mass stars between roughly 0.5 and 8$M_{\odot}$ are thought to evolve through the AGB. During this phase, they develop individual shells of helium and hydrogen undergoing fusion simultaneously. The interaction between these shells creates a distinctive cyclic process where sudden ignitions in the helium fusing shell around the inert carbon-oxygen core send pulses of energy outward and allow convection to enrich the surface with newly-synthesized carbon and nitrogen, as well as heavier s-process metals if the star is massive enough. During these thermal pulses, the temporarily unstable outer layers experience considerable radiation pressure which drives a strong stellar wind, leading to significant mass loss (Höfner & Olofsson 2018) and enriching the local interstellar medium.

Stars evolve through the AGB period very quickly – on the order of 100,000 years – and for this reason the initial size and metallicity of stars that will enter the AGB phase is difficult to confirm with observations. Further complicating matters, models of AGB stars vary widely as many physical aspects are not known from first principles and must be described by semi-empirical calibrations (Kippenhahn et al. 2012). The differences between models lie primarily in the treatment of convection, from handling the convective instabilities to the chosen size of the mixing regions, which in turn dictate the physical and chemical evolution during the AGB phase (Ventura & Marigo 2010). The challenging nature of both modeling and observing renders the mass loss they experience and consequently the production of metals which reach the ISM highly uncertain.

Dataset	Masses (total #)	Metal Mass Fractions (total #)	Code	α_{MLT}	RGB $\dot{M}$	AGB $\dot{M}$
Cristallo et al. 2015	1.3-6 (8)	0.0001 - 0.02 (10)	FUNS	2.0	$\eta = 0.4$	S06
Choi et al. 2016	0.5-8	0.000001 - 0.04	MESA	1.82	$\eta = 0.1$	Dutch/B95 ($\eta_B = 0.2$)
Karakas & Lugaro 2016	1-8 (21)	0.007 - 0.03 (3)	Monash	1.86	None	VW93
Ventura et al. 2018	1-8.5 (17)	0.014 (1)	ATON	(FST)	None	B95 ($\eta_B = 0.02$)
Karakas et al. 2018	1-7 (20)	0.0028 (1)	Monash	1.86	None	VW93/B95 ($\eta_B = 0.02$)
Battino et al. 2022	1-7 (8)	0.0001 - 0.03 (6)	MESA/PPN	2.0	$\eta = 0.5$	B95 ($\eta_B = 0.01/0.02$)
This work	0.8-7 (12)	0.0001 - 0.03 (10)	MESA	Scaled	$\eta = 0.5$	B95 (Scaled)

Table 1. Grid details for this work and several other AGB numerical modeling studies. VW93 = Vassiliadis & Wood 1993, B95 = Blöcker 1995, S06 = Straniero et al. 2006, FST (Full Spectrum of Turbulence) = Canuto & Mazzitelli 1991.

1.2 Mass Loss

Mass loss is the defining feature of AGB evolution, but the physical processes in these stars are non-trivial and remain a primary source of uncertainty when modeling (Karakas & Lattanzio 2014). The mass loss rate impacts not only the star's lifetime, but the opportunities for nucleosynthesis in different interior layers and the potential for dredging up heavier elements to the surface and promoting ISM enrichment. The star's luminosity drives the mass-loss rate, but the efficiency with which it does so depends to an uncertain extent on a secondary factor, its metallicity.

Counterintuitively, AGB mass-loss rates decrease with increasing initial metallicity. Generally, metals in stars create inhomogenous opacities and complicate convective mixing, leading to more photon absorption and scattering and greater radiation pressure. This outward pressure creates stellar winds and encourages mass loss. In AGB stars, however, the thermal pulsing activity is greater with lower metallicity because the reduced radiation pressure leads to a larger and hotter core. The helium shell surrounding a larger core experiences stronger helium flashes which results in more dramatic expansion and contraction of a star's outer layers which accelerates mass-loss (Höfner & Olofsson 2018). This kind of unusual behavior in AGB stars continues to challenge modelers.

The traditional approach uses empirical formulas, starting with the Reimers treatment for the red giant branch (RGB) (Reimers 1975) which relates the mass-loss rate to the stellar luminosity, radius, and mass. A revised approach was later developed by Blöcker 1995 to handle the more rapid mass loss observed in the AGB by modifying Reimers' formula to make it more sensitive to luminosity. These seminal mass-loss laws control both the metal yields and the likelihoods that the numerical AGB models will successfully progress through the complex thermally pulsing phase. A key question is determining whether models of AGB stars that manage to numerically navigate their evolution also agree with observations.

1.3 Metal Yields

Outstanding questions related to metal yields continue to arise. Carbon IV, an ion popular with high-redshift observers, is underpredicted by 10-50× in models compared to observations (Rahmati et al. 2016) even when other ions and observables such as HI reionization history and the galaxy stellar mass function match observations well (Finlator et al. 2020; Huscher et al. 2024). Observational surveys are finding considerable numbers of carbon-enriched metal poor stars

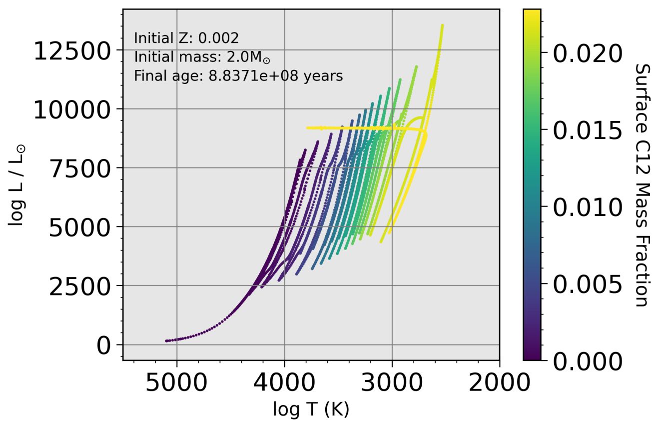

Figure 1. The AGB phase of the HR diagram from the model with initial mass 2 $M_\odot$ and initial metal mass fraction 0.002. The progression of thermal pulsing leads to increased carbon at the star's surface.

(Hansen et al. 2023) and efforts to model these have shown discrepancies between predicted and observed carbon abundances (Campbell & Lattanzio 2008; Chiaki et al. 2020). Recent JWST observations have also revealed extremely high N/O ratios in galaxies at z>10, which is surprising because such young, low-metallicity stellar populations are not expected to produce large amounts of nitrogen so early in cosmic history (Nakajima et al. 2023). Either rapid or unusual nitrogen production processes might be possible at early times, or there are nitrogen enrichment pathways yet undiscovered. Updating stellar enrichment timescales and yield tables of nitrogen and carbon informs these problems.

AGB stars going through thermal pulsing activity are a major source of lighter metals through the CNO cycle and heavier metals through slow neutron capture. Stellar winds carry this material away from the star, allowing it to cool and condense into dust. While moderate producers of alpha elements like oxygen and magnesium, it is thought that AGB stars are one of the primary sources of cosmic carbon (Herwig 2000). It has been estimated that one third of a galaxy's carbon is produced by AGB stars, providing roughly the same amount as core-collapse supernovae and Wolf-Rayet stars (Karakas & Lattanzio 2014). Since stellar carbon yields are difficult to measure observationally, we must rely on stellar evolution modeling to estimate the amount of carbon they produce. There is still much uncertainty in the carbon production from AGB stars of different masses and metallicities due to the difficulty in simulating these stars and comparing the results to observations (Karakas & Lattanzio 2014).

Many quality models of AGB stars and their associated metal yields have been published, including Cristallo et al. 2015, Choi et al. 2016, Karakas & Lugaro 2016, Ventura et al. 2018, and Battino et al. 2022. These works focused on specific ranges of stellar mass and metallicity (see Table 1), and employed different opacity tables and convection and mass-loss treatments. To examine specific AGB phenomena such as hot bottom burning or pockets of ^{13}C, modeling studies often focus on a range of masses at one or few metallicities, or a range of metallicities at few masses, to address their questions. Theoretical efforts rarely survey a comprehensive suite of stellar masses and metallicities (see, however, Choi et al. 2016).

Further motivation is found with large-scale cosmological simulations like EAGLE and Technicolor Dawn which have derived mass-loss rates from the Bruzual & Charlot 2003 population synthesis models and metal yields from a disparate collection of studies spanning different metallicities (Oppenheimer & Davé 2008). This approach with broad stellar population characteristics and incongruent AGB modeling was developed because a consistent grid of individual models of stellar evolution predicting mass loss rates over a broad range of initial masses and metallicities was not available. The feedback prescriptions of these cosmological simulations will improve by incorporating updated internally-consistent tables from modeling AGB stars with first principles, replacing the coarser stellar population averages.

Calculations of galactic chemical evolution also directly rely on stellar yields (Tinsley 1980; Karakas & Lugaro 2016; Johnson & Weinberg 2020). The metal yields attained from models of AGB stars can vary depending on choices made in the numerical calculations such as the mixing lengths, the reaction network, and treatment of mass loss (Ventura & D'Antona 2005). Ideally, chemical evolution modelers would have a self-consistent set of AGB stellar yields covering a range in initial mass from ∼0.8 $M_\odot$ to the limit for core collapse supernovae, ∼10 $M_\odot$, for all elements up to the heaviest s-process element, and for a broad range of initial metallicities (Karakas & Lattanzio 2014).

We take a determined step in this direction by modeling AGB stars from 0.8 to 7M$_\odot$ at a large range of metal mass fractions from nearly metal-free (Z=0.0001) to supersolar (Z=0.03), and with a reaction network involving 16 species up to silicon (A=28). In Section 2, we describe how we run the models and our approach to managing convection, mass loss, opacities and yields. In Section 4, we discuss the observations we test against and differences to existing models. In Section 3, we review the results and caveats of our findings. Finally, we provide our conclusions and links to access the mass loss and yield tables in 5.

2 STELLAR MODELING

2.1 Overview

We run a suite of models with Modules for Experiments in Stellar Astrophysics (MESA Paxton et al. 2011, 2013, 2015, 2018, 2019; Jermyn et al. 2023) in a range of initial stellar masses and metallicities. MESA is a powerful open-source software package that calculates one-dimensional stellar evolution models with many available initial parameters and is frequently updated to incorporate improvements to key modules including opacity tables, reaction networks, and output formats.

	Z		
$M_\odot$	0.0001	0.015	0.03
0.8	0.004	0.019	0.023
1.0	0.005	0.024	0.029
1.5	0.008	0.035	0.044
2.0	0.011	0.047	0.058
2.5	0.013	0.059	0.073
3.0	0.016	0.071	0.087
3.5	0.018	0.083	0.101
4.0	0.021	0.095	0.116
4.5	0.024	0.106	0.131
5.0	0.026	0.118	0.145
6.0	0.032	0.142	0.175
7.0	0.037	0.165	0.204

Table 2. Subset of Blöcker scaling factors (η_B) used in the stellar models which are a function of initial stellar mass and metallicity: $\eta = \frac{M}{12M_\odot} \times Z^\beta$ where $\beta = 0.3$ for all models except for Z=0.03 of the 4 largest masses it is $\beta = 0.2$.

We model a grid of 120 stars evolved through the AGB with these key details:

(i) **Masses**: 12 initial stellar masses from 0.8 to 7M$_\odot$
(ii) **Metal mass fractions**: 10 initial metal mass fractions from 0.0001 to 0.03
(iii) **Mass loss**: treatment from Blöcker 1995 with a scaling factor (η) adjusted by a calibrated power law (Table 2) ranging from 0.004 - 0.204.
(iv) **Mixing length**: adjusted parameter (α_{MLT}) by a calibrated linear scale ranging from 1.7 - 2.3.
(v) **Opacity tables**: New observationally-calibrated opacity tables at low temperature (Magg et al. 2022) and high temperature (Farag et al. 2024).
(vi) **Reaction Network**: 60 individual reactions covering 16 isotopes from ^{3}He to ^{28}Si.
(vii) **Instability management**: Management of Fe Peak and Hydrogen Recombination instabilities as well as automated variation control developed by Rees et al. 2024 to navigate complex thermal pulsing behavior.

We set out to generate a consistent grid of models that will be useful in a wide array of applications, from cosmological simulations to galaxy chemical evolution models. Table 3 shows the details of each model, with its associated scaling factors and mixing lengths.

2.2 Running the Models

We create a pre-main sequence model of uniform composition and contraction and evolve it through the AGB phase. The internal convective and radiative processes evolve significantly as a star ages, so we isolate five stages which are run with different MESA parameters: 1) main sequence, 2) red giant branch, 3) horizontal branch, 4) asymptotic giant branch (before pulsing begins), and 5) asymptotic giant branch with thermal pulsing.

These external parameter files are uniform for all models, with only the initial mass and initial metallicity being altered

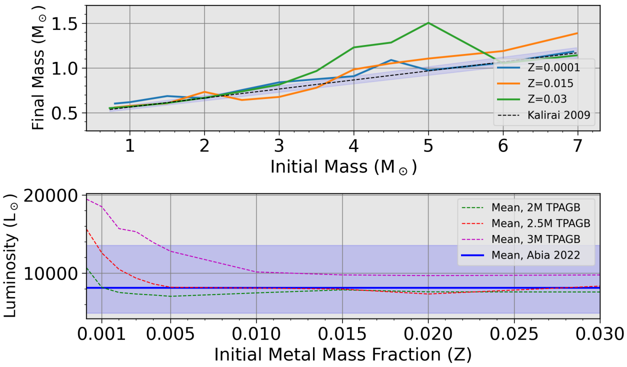

Figure 2. (Top) The initial mass of our models as a function of the final mass they reach. For comparison, observations are included from Kalirai et al. 2009 of this relation in white dwarfs residing in nearby Milky Way globular clusters. (Bottom) Time-averaged luminosities of our 2M, 2.5M, and 3M models throughout the TP-AGB as a function of their initial metal mass fraction. These masses encompass most of the carbon stars that would exist in a population such as the one studied by Abia et al. 2022 and show good agreement with the average luminosity for their carbon star population which is the horizontal blue line with the associated error.

between them. Routines to assign the scaled values for mixing length (α_{MLT}) and mass loss scaling factor (η_B) are written into the MESA executable via the "run_star_extras.f90" file. The models are allowed to run until either the envelope mass reaches 0.005 M$_\odot$ remaining or the progress reduces to a change in mass of 1e-6 M$_\odot$ in 1000 timesteps.

The rapid transitions in pressure and temperature at the boundaries between layers of core, shell, and intershell regions can greatly hinder numerically solving the differential equations of state and are the primary difficulty in modeling thermal pulsing activity. To aid in navigating these areas, we employ the custom routine developed by Rees et al. 2024 to monitor and adjust the spatial and temporal resolution during the third dredge-up. This approach carefully eases or tightens the variability allowed in the equation of state solutions at each timestep which greatly improves progress through volatile periods in the model.

2.3 Convection

The treatment of convection is a crucial element in modeling AGB stars. Modeling the transport of energy by convection in stellar interiors in three dimensions is an enormously complex task (Henyey et al. 1959). Even a simpler 1D model has considerable challenges, particularly when handling convection in the presence of arbitrary abundances of metals impacting the opacity in localized regions. The classic approach to managing stellar convection is called Mixing Length Theory (MLT; Vitense 1953). The theory assumes the convective process is driven by parcels of buoyant fluid that travel a distance before dissipating. This distance, as well as the nearby pressure scale height, is represented by the key MLT parameter α_{MLT}. Higher values of α_{MLT} will permit models to have more efficient convective energy transport, while lower values will have less efficient convection and shallower temperature gradients.

We agree with VandenBerg et al. 2000 and Rees et al. 2024 that there is no evidence to suggest this efficiency would be constant for all stellar masses, arbitrary compositions, and at different stages of a star's evolution. Observations have shown the need for a metallicity-dependent mixing length with metal-poor giants in globular clusters requiring higher α_{MLT} values to match asteroseismic constraints (Tayar et al. 2017). Indeed, we find that lower metallicity stars often require larger mixing length parameters to avoid numerical instabilities. It has also been shown by 3D radiative hydrodynamic models that α_{MLT} decreases with increasing initial Z (Trampedach et al. 2014; Magic et al. 2015). A range of α_{MLT} from 1.7-2.3 is suggested by Magic et al. 2015 based on their calibration of values which best matched the adiabatic entropy of the convecting envelope for each metallicity in their models. To calibrate to these works and to confirm the potential of a varying convective efficiency, we scale α_{MLT} as a linear function of initial metallicity:

$$\alpha_{MLT} = 2.3 - [20 \times (Z_i - 0.0001)] \tag{1}$$

This α_{MLT} parameter addresses convective behavior in the sizable zones of a star undergoing convection, but the treatment of convection also requires meticulous attention at the boundaries of interior layers which experience the most unstable gradients in temperature and pressure and can quickly crash numerical models. This remains a major uncertainty when numerically modeling AGB stars (Karakas et al. 2022). Overshoot is a common approach to managing the convective boundaries, allowing buoyant parcels to approach a convective boundary and penetrate into the formally stable region.

We implement an established scheme for this extended convective mixing where the convection efficiency declines exponentially with the geometric distance from the layer boundary (Herwig 2000). The primary zone requiring this treatment is the bottom of the convecting envelope which is not only a location of significant numerical instability, but the efficiency of mixing here directly impacts the strength of a dredge-up event and the frequency of thermal pulses which changes the amount of metals that reach the star's surface. The boundary between the helium-burning shell and the inert core also requires custom overshoot values to ensure numerical stability.

Characterizing the results of these convective parameter choices call for another parameter, the dredge-up efficiency (λ), which is useful to describe how much intershell material is being brought up into the stellar envelope. This value is often between 0.5 and 1. A λ value greater than one means the third dredge-up is so strong it actually reduces the core mass from what it was before the pulse. We show the λ for each model in Table 3.

2.4 Handling Mass Loss

Both the Reimer and Blöcker mass loss treatments discussed in Section 1.2 employ a scaling factor parameter (η) to allow the mass loss rates to be adjusted and tuned to observations. This impacts the stellar model in many ways, from the number of thermal pulses that occur to unexpected (and unrealistic) paths in the star's stellar evolution as reflected by their Hertzsprung-Russell diagrams.

We use both mass loss treatments. Reimers' is at work when the star is on the RGB and continues while helium is present in the core, with a constant η_R of 0.5 in all models.[1] When the central helium abundance nears zero, Blöcker's treatment is engaged. We implement a variable Blöcker scaling factor (η_B) as a function of initial mass and metallicity:

$$\eta_B = \frac{M_i}{12M_\odot} \times Z_i^{0.3} \tag{2}$$

This scaling allows stars of greater mass to lose mass more readily, a necessity both for reasonable stellar lifetimes and likelihood for the numerical models to reach white dwarf masses. It also allows for metal-rich stars to lose mass more readily which accounts for their higher opacity and stronger radiation-driven winds. It is worth noting that studies have suggested that metal-poor carbon stars, whose overall metallicity is very low but atmosphere contains more carbon than oxygen, may have similar mass-loss rates to metal-rich stars of similar masses (Mattsson et al. 2008). Preliminary runs of low metallicity in our grid, however, have led us to include initial metallicity as a factor in varying η_B.

An additional advantage of this approach is that it does not require editing of MESA inlist files for every individual model. Incorporating Equation 2 into supplementary Fortran routines and rebuilding the executable allows all models to run with fewer manually-edited parameters saving time and reducing error in preparing the grid. These routines are provided with the metal yields and inlist files in the supplementary data.

2.5 Opacities

Radiative opacities at high temperatures are calculated from the Los Alamos OPLIB database (Colgan et al. 2016) and made available in MESA by Farag et al. 2024. These tables provided the tremendous range in metallicity required for this study. We adopt the solar-scaled abundance mixture constructed from photospheric estimates of the solar heavy element abundance (Magg et al. 2022). Low temperature opacity tables, also using the solar-scaled abundance mixture of Magg et al. 2022 have been computed with the approach of Ferguson et al. 2005 and included in MESA r24.08.1.

2.6 Calculating the Yields

Each model employs a reaction network which includes 16 species: ^{1}H, ^{3}He, ^{4}He, ^{12}C, ^{13}C, ^{13}N, ^{14}N, ^{15}N, ^{16}O, ^{17}O, ^{18}O, ^{19}F, ^{20}Ne, ^{22}Ne, ^{24}Mg and ^{28}Si. MESA records the abundances of these species at the surface with each timestep which we use to produce the final isotope yield. Note that "yields" in the literature sometimes refer to the net production in relation to the star's initial abundance – where the net can be negative – and other times "yields" represent the total amount the star expels. Here we adopt the latter, calculating the ejected mass rates of each species from the stellar surface by multiplying the change in stellar age between timesteps (years) by the change in mass ($M_\odot$/year) and by the surface fraction of carbon and summing the result at each timestep:

$$M_i = \int_0^\tau X_i \frac{dM}{dt} dt \tag{3}$$

where M_i is the total mass ejected from the star of element i, τ is the total stellar lifetime, X_i is the current mass fraction of the species at the star's surface, and $\dot{M}$ is that timestep's

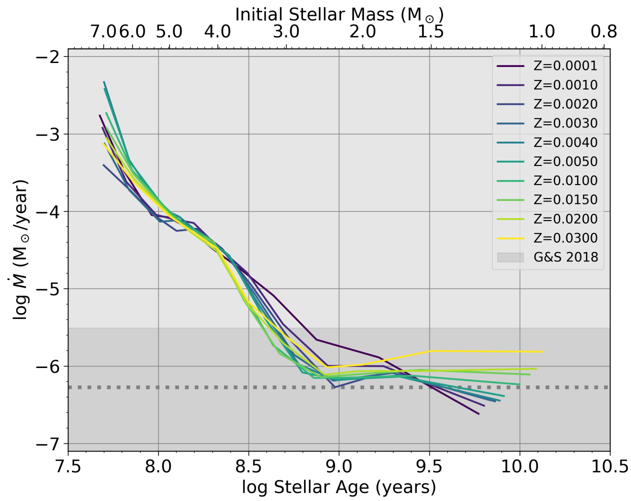

Figure 3. Mass loss rates of the MESA models as a function of the AGB star's age, calculated by integrating the mass loss rate during pulsing and dividing by the duration. For each initial metal mass fraction (i.e. Z=0.015), the mass loss rates are interpolated in initial stellar mass to provide rates at a fine series of stellar ages. The top axis indicates the initial stellar mass which would pass through the AGB phase at the corresponding stellar age. The mass loss rates found by Groenewegen & Sloan 2018 from carbon stars in the Local Group are represented by the gray dotted line (average) and dark gray area (range).

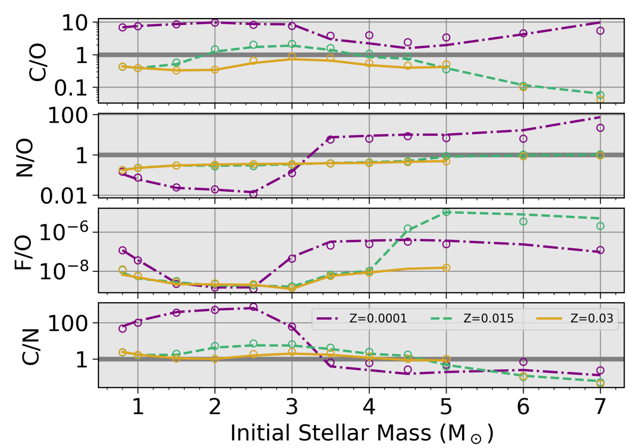

Figure 4. Lines are the mass ratios of total yields as a function of initial stellar mass after the last thermal pulse. Dots are the ratio of the final surface mass fraction after the last thermal pulse.

[1] Tiny adjustments to η_R were beneficial to progress through TPAGB in a handful of high-mass high-metallicity models.

mass loss rate. This is the total yield ejected from the star and is always positive.

3 RESULTS

We model 120 stars at a range of masses and metallicities, guiding them through the AGB while maintaining stable thermal pulsing activity until the helium in the core is depleted or the model has progressed as far as possible.

Figure 1 zooms in on the AGB stage of one of the 2M$_\odot$ models with the colorbar representing surface Carbon 12 abundance. The distinct cycle of thermal pulses coincides with changes in luminosity as the star cools and with each pulse, more metals such as carbon are dredged-up to the stellar surface. As shown in this example, we allow the models to evolve if possible until the entire envelope is lost and the transition to a white dwarf begins as the indicator that the AGB phase is complete.

3.1 Mass Loss Rates

In Figure 3, we present the mass loss rates of our models after interpolating in mass to effectively capture the AGB star that undergoes thermal pulsing at every stellar age, in between the ages of the earliest onset (from 7M$_\odot$ stars) to the latest (from 0.8M$_\odot$ stars). Low metallicity models continue to lose mass more slowly as they progress through the AGB, but models with more metals reach a constant mass loss rate after $\sim 10^9$ years, and at very high metallicity it can even increase after this age. We assume the age of 10^9 years reflects the point in a stellar population where longer-lived lower mass stars take over the returning of mass and metals to the ISM. Lower mass stars with more metals lead this charge due to higher opacity building up radiation pressure which expands the envelopes and lowers the surface gravity, thus allowing mass-loss to proceed more rapidly.

We include the initial stellar masses on the top axis to denote the mass which is comparable to the age at which those masses undergo the thermally pulsing AGB phase. A 7M$_\odot$ star, for example, quickly passes through the AGB when it is log(age/yr) = 7.7 (∼50 million) years old.

3.2 Yields and Ratios

Specific treatments for convective mixing, overshooting, and mass loss influence AGB models and result in different metal yields and surface ratios. Table 3 shows some of these model choices, notably the convective mixing length and RGB and AGB mass loss parameters, between different studies. The resulting surface metal yields from our models are greater by ∼50× at most stellar masses, for example, from Choi et al. 2016 (MIST), which is likely due to their large constant Blöcker scaling factor leading to rapid mass loss limiting thermal pulsing activity. In the same way, we see ∼5× higher yields at most masses than Cristallo et al. 2015, who employed different AGB mass loss based on pulsation periods (Straniero et al. 2006), and did not employ overshoot between convective boundaries.

The total metal yields of standard isotopes expelled from the stars are shown in Figure 5 (additional isotopes in Appendix A1) with comparisons included from Karakas 2010 and Karakas & Lugaro 2016. Carbon 12 peaks at the same mass but half the abundance at Z=0.0001, peaks at a lower mass (3M$_\odot$) and comparable abundance at solar metallicity, and at the same mass (3.5M$_\odot$) for supersolar metallicity models. Nitrogen 14 shows excellent agreement at high metallicity, but is considerably lower at the other metallicities. Oxygen 16 and Neon 20 match well between the two studies. Magnesium 24 yields show a considerable increase in our models over Karakas & Lugaro 2016 and Battino et al. 2019.

Figure 4 shows surface ratios of carbon to oxygen (C/O), nitrogen to oxygen (N/O), fluorine to oxygen (F/O), and carbon to nitrogen (C/N) at low, solar, and high metallicity for all masses. These ratios are important metrics for AGB stars because they reveal the efficiency of the internal dredge-up processes and hint at the chemical imprint these stars make on their host galaxies.

Each dredge-up event mixes carbon from the helium shell up into the envelope which increases the carbon ratios at the surface, that is until stars with sufficient mass reach temperatures at the base of the convective envelope to fuse carbon into nitrogen (Karakas & Lattanzio 2014). Figure 4 shows dips in C/O and C/N starting at 2.5M$_\odot$ with a corresponding increase in N/O, a sign that this process, known as hot bottom burning (HBB; Sackmann & Boothroyd 1992, Blöcker et al. 2000), has begun. While this is a lower threshold mass for HBB than the $\sim 4-4.5M_\odot$ found by other studies (Karakas & Lattanzio 2014; Boothroyd et al. 1995), it has been shown that lower metallicities experience HBB at lower masses (Ventura & Marigo 2010) and we do see the trends most pronounced in the Z=0.0001 models. This is expected from the combination of implementing exponential overshoot and our scaled α_{MLT}, which is higher particularly at low metallicities, leading to more efficient convection and higher temperatures at the base of the envelope.

The surface C/O ratio merits special attention as the primary observational diagnostic for AGB stars because it directly reflects the competition between third dredge-up which enhances carbon and hot bottom burning which destroys carbon (Straniero et al. 2023). This ratio determines whether stars appear as oxygen-rich M giants or carbon-rich C stars (hereafter "carbon stars") in photometric surveys, making it a crucial parameter for interpreting stellar populations in different metallicity environments. In the Magellanic Clouds where metallicities are on the order of Z=0.005 (Davies et al. 2015), stars of masses as low as 1.5M$_\odot$ have been found to become carbon stars (Ventura et al. 2016), and at higher metallicities, this minimum mass shifts up to 3-4M$_\odot$ (Karakas & Lattanzio 2014). Solar metallicity models surpass C/O=1 at $\sim 1.75M_\odot$ and become carbon stars, though stars with $Z \geqslant 0.02$ never reach C/O=1, with so much initial oxygen present. Very low metallicity models ($Z \sim 0.0001$) are carbon-rich at all masses in the TPAGB.

The N/O ratio gently increases in stars with solar or greater metallicity as initial mass is increased, suggesting active but moderate HBB producing additional nitrogen. N/O jumps up enormously, however, as HBB in low metallicity stars with much lower opacity in the envelope leads to more vigorous HBB. This presents an intriguing consideration for recent observations of high N/O ratios at high redshift (Charbonnel, C. et al. 2023). A high N/O is possible even with little initial metals if star formation began early enough and a

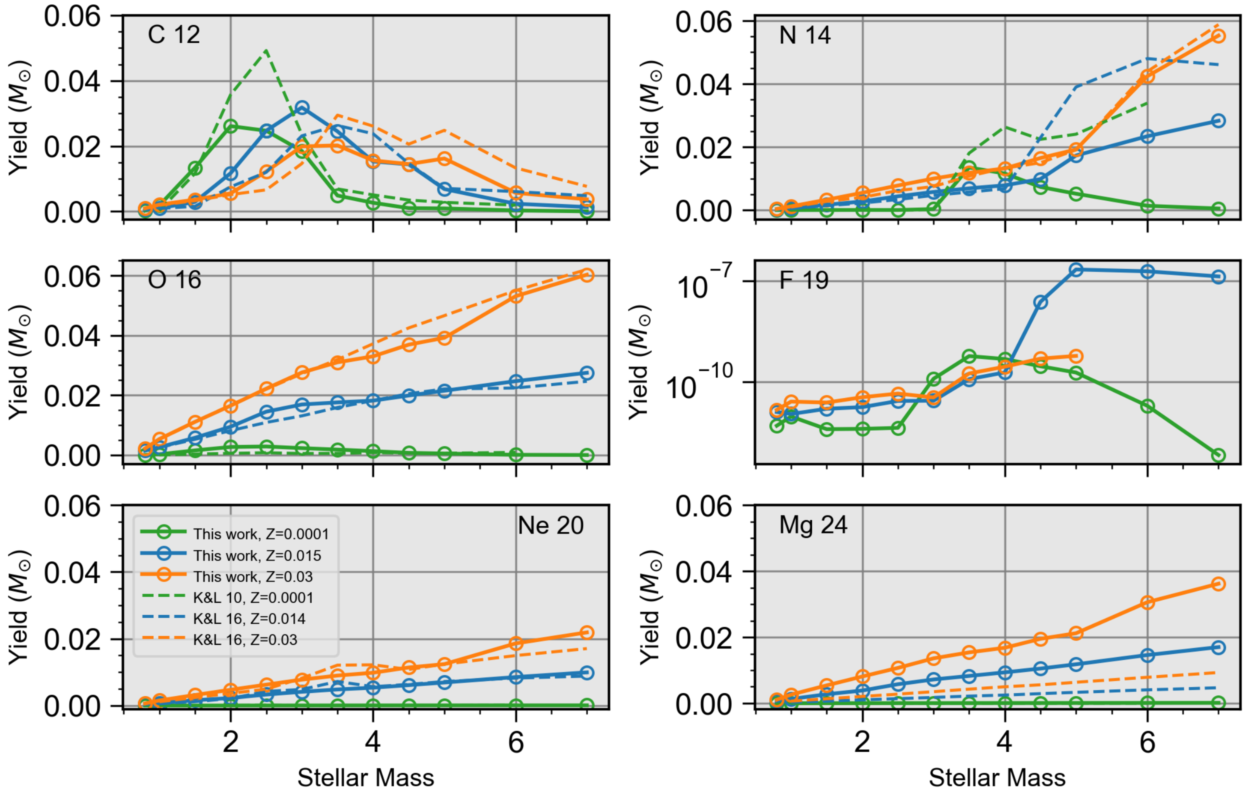

Figure 5. The ejected C12, N14, O16, F19, Ne20, and Mg24 yields as a function of initial stellar mass for 3 initial metallicities: nearly metal free (0.0001), solar (0.014 or 0.015), and supersolar (0.03), with Karakas & Lugaro 2016 results for comparison.

top-heavy initial mass function at early times produced considerable stars with HBB-capable masses.

Fluorine is produced during thermal pulsing in AGB stars, but it is also fragile and easily destroyed by numerous reactions in stellar interiors (Jorissen et al. 1992). Here we see F/O follow a similar trend as N/O, which is expected as the main fluorine production reaction requires nitrogen so it should increase or decrease with nitrogen availability (Abia, C. et al. 2015). We note, however, that only the solar metallicity models (green dashed) are reaching the $\sim 10^{-4} - 10^{-5}$ levels found by others in both observations (Lucatello et al. 2011) and models (Lugaro et al. 2004; Karakas 2010). At Z=0.0001, the very low metallicity allows temperatures in the He shell of $> \sim 10^8$K, which destroys fluorine. The Z=0.03 models should not have this problem, but we scale the mixing length (Formula 1) inversely with metallicity, so they will experience a weaker dredge-up efficiency impacting the fluorine that reaches the surface.

The C/N ratio shows the most distinct signature of HBB, with a reversal at $\sim 2.5 M_\odot$ where the trend changes from increasing C/N due to carbon dredge-up in lower mass stars to sharply decreasing C/N as hot bottom burning converts the newly-dredged carbon into nitrogen.

Figure 4 includes both the ratio of total yields over the star's lifetime (lines) and the ratio of surface mass fraction at the end of TPAGB (dots). While similar, the dots of surface mass fraction are generally slightly above the yields for C/O showing that most of the carbon enrichment happens late in the TPAGB. A slight opposite trend can be seen with N/O suggesting that the surface reflects the late time when pulsing has slowed and HBB is over. The final F/O ratio at the surface falls considerably below the integrated yields, particularly for low-metallicity, higher-mass models experiencing vigorous HBB. This suggests that fluorine, unlike carbon which is dredged up late in the evolution, may be consumed by the hot bottom burning process, making the surface abundance a poor tracer of the total fluorine production during the AGB phase.

4 COMPARISON TO PREVIOUS RESULTS

4.1 Observational Tests

To test our models' output reasonably reflects AGB observations, we start by comparing the final core masses of our models with white dwarf mass observations from nearby clusters. Kalirai et al. 2009 studied such white dwarf populations found by photometric surveys and followed up with spectra to ascertain their spectral type and progenitor mass. By isolating a sample of white dwarfs from different clusters with a spread of initial stellar masses, they develop an empirical fit to the final-initial mass relation. The top panel of Figure 2 shows the white dwarf mass distribution found by Kalirai et al. 2009 in good agreement with the final-initial mass relation of our models at 3 different metallicities.

Next, while the strength and frequency of an AGB star's thermal pulses can be changed readily in models with the parameters related to mixing length, mass loss, and convective overshoot, we cannot calibrate this pulsing activity directly to observations because the pulse cycle is tens to hundreds of thousand years, too long to observe in real-time. It is possible, however, to constrain AGB models with observations of the measured luminosities of carbon stars, as done by Osborn et al. 2024. Carbon star population studies at a range of masses and metallicities provide bolometric magnitudes which can guide numerical models. Abia et al. 2022 confirmed thousands of carbon stars from the Gaia survey and based on the measured luminosities and kinematics concluded that they constitute a mix of stellar types with a wide range of metallicities. These data provide a baseline of luminosities from observed AGB stars to validate our grid of MESA models.

Abia et al. 2022 finds an average bolemetric luminosity of -5.04 ± 0.55 mag which corresponds to $\sim$8200$L_\odot$. The minimum mass we run in our grid at solar metallicity that becomes a carbon star, that is which has a surface C/O ratio greater than 1, is 2$M_\odot$. Weighting a population by a standard $M^{-2.35}$ initial stellar mass function leaves the bulk of the carbon stars near this $2M_\odot$ initial mass. We therefore develop our scaling of mixing length α and Blöcker scaling factor η (Equations 1 and 2) to both encompass ranges described in Sections 2.3 and 2.4 and to realize an average luminosity close to 8200$L_\odot$ mag throughout the TP-AGB in the 2$M_\odot$ and 2.5$M_\odot$ models to capture the majority of carbon stars in the Abia et al. 2022 population. Figure 2's bottom panel shows these observed metrics alongside the luminosities of our IMF-weighted models at each initial metallicity.

Finally, observations of mass loss rates from different populations of pulsating AGB stars have found values of $10^{-7}M_\odot$/year to $10^{-5}M_\odot$/year (Groenewegen et al. 2009; Groenewegen & Sloan 2018). While these studies encompass a wide range of stellar characteristics and are non-trivial measurements with considerable uncertainties, they provide a valuable sanity check that our treatment of mass loss, and in particular the chosen scaling factors, provides reasonable mass loss rates within these values. The top panel of Figure 3 shows mass loss rates of our models after integrating over the TPAGB and then dividing by the duration. This is a necessary step to accurately reflect the wildly fluctuating behavior experienced during this phase (see Figure 1). The rates are then interpolated in stellar age to capture the mass loss rates of stars with intermediate masses between our models. The bulk of the mass loss rates fall neatly in between the 10^{-7} to $10^{-5}M_\odot$/year expectation, with the exception being the early onsetting TPAGB of the higher mass stars which peak at $10^{-2.5}M_\odot$/year. The average mass loss rate from carbon stars studied by Groenewegen & Sloan 2018 ($5.32 \times 10^{-7}M_\odot$/year) is included as a horizontal dotted line which matches our models well, especially considering the observations will be dominated by the more numerous longer-living stars.

4.2 Updating Cosmological Simulation Inputs

One motivation for updating the AGB yield tables is the considerable discrepancy between the abundance of C IV produced by modern cosmological simulations and the abundances seen in observations. Rahmati et al. 2016 compared simulated C IV from Illustris and EAGLE to a variety of observational studies and showed that, while the abundances match well at low redshifts, they are 10-50× less at redshifts earlier than z=3.5. Even Technicolor Dawn , a simulation which accommodates for spatial variations in the ionizing background, has the same result (Finlator et al. 2020). This is puzzling, and raises the question whether simulations are underproducing carbon, underionizing the carbon, or some observational bias is overestimating the carbon abundances that were present in the early Universe.

The Technicolor Dawn and EAGLE simulations both derive their AGB mass outflow rates from the Bruzual & Charlot (2003) population synthesis model, which in turn employs stellar evolution tracks from Bressan et al. 1993 across different masses and metallicities (Oppenheimer & Davé 2008). Metal yields from a variety of theoretical models are then folded into this framework to cover a wide metallicity range (Marigo 2001; Herwig & Austin 2004; Gavilán et al. 2005), finally producing lookup tables of overall stellar mass and metal yields for AGB-produced carbon, nitrogen, and oxygen.

Figure 7 compares the existing tables used by Technicolor Dawn and EAGLE with the results of our grid of models. The bottom two panels show that the instantaneous carbon metallicity of the outflowing gas is similar across stellar ages and initial metallicities, just noting a 2× reduction at sub-solar metallicities in our models. The top 2 panels, however, show a drastic disparity in the instantaneous mass loss rates at all ages and metallicities. The rates of mass loss in our models are $\sim$100× stronger, a striking result with considerable implications for not only the CIV underproduction problem, but other trends in galactic chemical evolution. The amount of disparity is surprising, but Karakas & Lattanzio 2014 point out that while total yields remain similar between models, mass loss prescriptions are much more variable. In addition, Marigo et al. 2020 observed that updated physics in AGB models leads to higher mass loss rates while maintaining similar nucleosynthetic yields.

4.3 Differences from other Models

Even minor adjustments to parameters such as the mixing length and mass-loss scaling factors result in considerable changes to the dredge-up efficiency in AGB models (Rees et al. 2024). One effective way to compare models is through the surface C/O ratio. C/O tells us not only about the composition of an AGB star's envelope but it encodes the dominant interior processes and is a key observable to classify stars and infer phases of mass-loss.

In Figure 6, the C/O ratio of our models is compared to the MIST models of Choi et al. 2016 (dashed) and those of Karakas & Lugaro 2016 (dotted). The MIST models, run with the MESA code like ours, show much less carbon at the surface at all initial metallicities and masses, suggesting weaker or fewer dredge-up events. This meets expectations of the Dutch mass loss scheme which can be more aggressive and lead to earlier cessation of thermal pulses and also removes envelope material that would otherwise be available to participate in the dredge-up process (Höfner & Olofsson 2018). The peak of carbon enrichment, however, does match the other models of intermediate metallicity at 3$M_\odot$. The less consistent trend at Z=0.0001 and nearly flat trend at Z=0.03 demonstrate the potential benefit of scaling the mixing length and mass loss parameters at extreme metallicities.

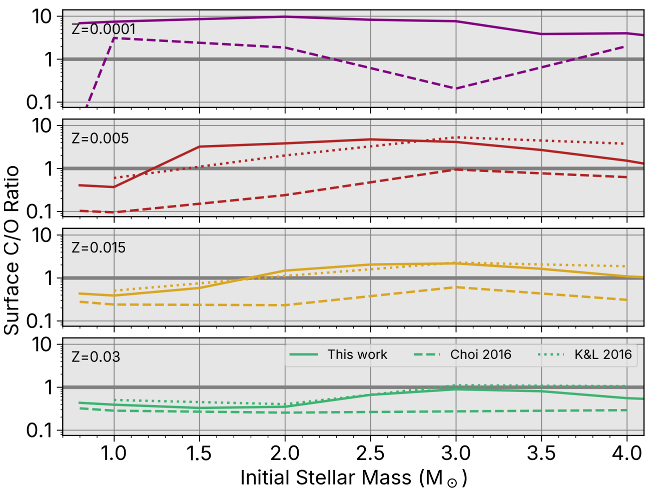

Figure 6. A comparison between different studies of the surface C/O ratio at the end of the AGB phase at (top) Z=0.0001, (second) Z=0.005, (second) Z=0.015, and (bottom) Z=0.03. Dashed lines are the result of MESA models from MIST (Choi et al. 2016), dotted lines are the results of Monash models from Karakas & Lugaro 2016, and solid lines are our models. The point where they surpass the thick grey horizontal line (C/O=1) is the stellar mass that becomes a carbon star.

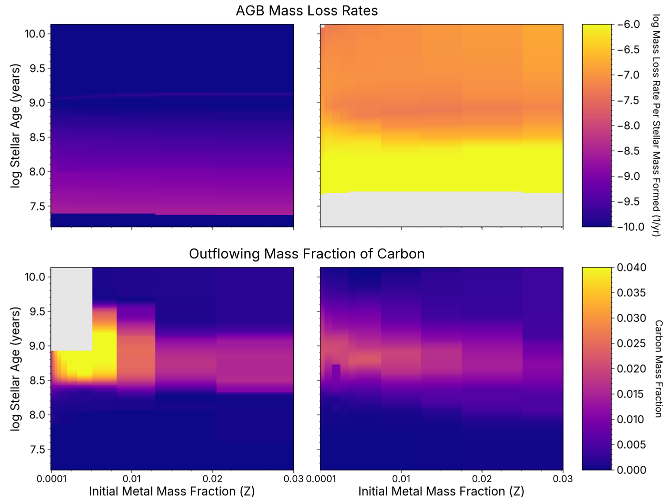

Figure 7. A comparison between the existing input tables for simulations such as EAGLE and TECHNICOLOR DAWN on the left and our results on the right, all weighted by a Chabrier IMF. (Top) Instantaneous mass loss rates of AGB stars as a function of their age and initial metallicity, normalized by the stellar mass formed. (Bottom) Same, but instantaneous carbon mass fraction of the outflowing gas from the AGB stars.

The Karakas & Lugaro 2016 models, though run with a different code and AGB mass loss treatment, showed comparable trends at solar and high metallicity. The main difference is the transition to a carbon star at Z=0.005 occurs at a larger mass of $\sim$1.5M$_\odot$ for them than we see at $\sim$1.25M$_\odot$.

We attribute these differences first to the variable mixing length α_{MLT}. The common practice of fixing mixing length and mass loss parameters for an entire grid of models is more for simplicity and computational limitations than realism. The change in efficiency of convection in lower metallicity stars with lower opacity versus higher mass counterparts has been demonstrated in 3D hydrodynamic simulations (Magic et al. 2015). The larger α_{MLT} at lower metallicities can explain the high C/O with Z=0.0001 models because it creates more efficient convection leading to deeper penetration of the convective envelope into the intershell region during dredge-up episodes.

Second, the recent OPLIB radiative opacity tables from Farag et al. 2024 show higher opacities in higher temperature regions, such as the active helium shell around cores of AGB stars, which could promote deeper convection. The wider range of these tables also provide improved accuracy of opacities at the near metal-free and twice-solar metallicity models we explore here.

In summary, the combination of metallicity-dependent mixing lengths and mass-loss parameters, layer-dependent exponential overshoot, and updated opacities produces AGB models with enhanced dredge-up efficiency compared to many previous models. While our approach requires more computational complexity, it provides a more physically motivated treatment of convection across a wide metallicity range relevant for galactic chemical evolution studies and large-scale cosmological modeling.

5 SUMMARY AND FUTURE DIRECTIONS

We run a grid of stellar models with MESA v24.08.1 at a mass range of 0.8 to $7M_\odot$ and an initial metal mass fraction range of 0.0001 to 0.03. We determine the stellar mass loss rates and the metal yields for 16 isotopes from these models. Finally, IMF-weighted input tables as functions of metal mass fraction and stellar age are generated and made available for cosmological simulations or other scientific applications.

We summarize several takeaways:

(i) Comparable luminosities and metal yields to previous AGB studies are possible with fewer thermal pulses
(ii) Total yields of Carbon 12, Nitrogen 14, Oxygen 16, and Neon 20 match previous studies well. Magnesium 24 yields are 3-4× greater at all initial masses.
(iii) The minimum initial mass for carbon stars derived via interpolation is $\sim 1.25 M_\odot$ for initial metallicity Z=0.0001, $\sim 1.75 M_\odot$ for Z=0.005, and $\sim 3 M_\odot$ for Z=0.03.
(iv) Metal yields match well with existing tables in use by EAGLE and Technicolor Dawn cosmological simulations. The rate of mass loss, however, may be considerably underestimated in these tables as our results show 50-100× stronger outflows from AGB stars.
(v) Scaling the convective mixing length by calibrating to 3D hydrodynamic simulations and the mass loss parameter to observed carbon star luminosities result in stable AGB models which align with observations.

Comparing the isotope ratios from our grid to broad stellar spectroscopic surveys like APOGEE would be an exciting follow up to this study. Within the models themselves, rotation is a property that has been shown to impact the convection and mass loss of Wolf-Rayet stars, and would be an interesting addition to models of AGB stars. Also, stars in binary systems experience tidal interactions and mass transfer which can affect the internal temperature gradients and alter their convection patterns. As binary systems make up a considerable portion of stars, accounting for these effects could be meaningful to derive accurate mass loss rates and carbon yields, which we would like to investigate in the future.

6 ACKNOWLEDGEMENTS

EH: Conceptualization, Investigation, Software, Visualization, Writing - Original draft; **KF**: Conceptualization, Supervision, Writing - Review & Editing; **JJ**: Conceptualization, Supervision, Software, Writing - Review & Editing.

EH would like to thank Amanda Karakas, Ben Oppenheimer, and James Johnson for insightful discussions. EH is supported by the NASA FINESST program, award #80NSSC24K1483. This work utilized resources from the New Mexico State University High Performance Computing Group, which is directly supported by the National Science Foundation (OAC-2019000) and the Student Technology Advisory Committee. KF and EH gratefully acknowledge support from STScI Program #HST-AR-16125.001-A. The Cosmic Dawn Center is funded by the Danish National Research Foundation.

7 DATA AVAILABILITY

We have prepared the full grid of stellar yield and isotope abundance data in individual ASCII files for easier assimilation by researchers, as well as example MESA inlists and the custom Fortran files with parameter scaling, on Zenodo through the following link: https://zenodo.org/records/XXXXXXX.

Table 3: Results of All MESA Models in this Work

Inputs				Results						
$M_{initial}$	Z	α_{MLT}	η_B	M_{final}	τ_{TPAGB}	$\#TPs$	$L_{TP,avg}$	$L_{TP,max}$	$T_{bce,max}$	λ_{max}
0.80	0.0010	2.282	0.008	0.590	1.25E+06	7	4.56E+03	1.10E+04	2.71E+06	0.05
0.80	0.0020	2.262	0.010	0.584	1.25E+06	8	4.36E+03	1.06E+04	2.47E+06	0.00
0.80	0.0030	2.242	0.012	0.579	1.04E+06	6	4.47E+03	1.02E+04	2.47E+06	0.00
0.80	0.0040	2.222	0.013	0.575	9.79E+05	6	4.83E+03	9.85E+03	2.49E+06	0.00
0.80	0.0050	2.202	0.014	0.572	1.07E+06	7	3.74E+03	8.92E+03	2.53E+06	0.01
0.80	0.0100	2.102	0.017	0.565	9.09E+05	6	3.83E+03	8.47E+03	2.56E+06	0.00
0.80	0.0150	2.002	0.019	0.560	8.25E+05	6	3.71E+03	7.82E+03	2.59E+06	0.00
0.80	0.0200	1.902	0.021	0.558	6.49E+05	5	4.03E+03	7.51E+03	2.49E+06	0.00
0.80	0.0300	1.702	0.023	0.553	4.23E+05	4	4.27E+03	6.68E+03	2.74E+07	0.00
1.00	0.0001	2.300	0.005	0.619	1.32E+06	10	6.26E+03	1.32E+04	4.66E+06	0.23
1.00	0.0010	2.282	0.010	0.604	1.12E+06	8	5.58E+03	1.19E+04	4.52E+06	0.18
1.00	0.0020	2.262	0.013	0.598	1.11E+06	8	5.38E+03	1.16E+04	4.19E+06	0.14
1.00	0.0030	2.242	0.015	0.595	1.19E+06	9	5.14E+03	1.15E+04	3.91E+06	0.10
1.00	0.0040	2.222	0.016	0.594	1.20E+06	9	4.74E+03	1.11E+04	3.55E+06	0.07
1.00	0.0050	2.202	0.017	0.593	1.05E+06	7	4.85E+03	1.09E+04	3.42E+06	0.03
1.00	0.0100	2.102	0.021	0.582	1.04E+06	8	4.41E+03	9.92E+03	2.94E+06	0.00
1.00	0.0150	2.002	0.024	0.577	8.74E+05	7	4.62E+03	9.17E+03	2.91E+06	0.00
1.00	0.0200	1.902	0.026	0.572	7.94E+05	7	4.87E+03	8.61E+03	1.35E+07	0.00
1.00	0.0300	1.702	0.029	0.568	5.75E+05	6	5.17E+03	8.01E+03	5.44E+07	0.00
1.50	0.0001	2.300	0.008	0.687	9.92E+05	12	8.86E+03	1.64E+04	8.20E+06	0.62
1.50	0.0010	2.282	0.016	0.620	1.03E+06	10	7.55E+03	1.37E+04	7.32E+06	0.58
1.50	0.0020	2.262	0.019	0.614	1.12E+06	10	7.09E+03	1.31E+04	6.83E+06	0.55
1.50	0.0030	2.242	0.022	0.610	1.19E+06	10	6.87E+03	1.19E+04	1.47E+07	0.52
1.50	0.0040	2.222	0.024	0.608	1.17E+06	10	6.74E+03	1.17E+04	6.48E+06	0.51
1.50	0.0050	2.202	0.026	0.606	1.25E+06	11	6.65E+03	1.18E+04	2.33E+07	0.49
1.50	0.0100	2.102	0.031	0.605	1.24E+06	12	6.17E+03	1.23E+04	2.95E+07	0.38
1.50	0.0150	2.002	0.035	0.606	1.17E+06	11	6.42E+03	1.19E+04	5.61E+07	0.21
1.50	0.0200	1.902	0.039	0.699	1.02E+06	11	9.04E+03	1.09E+04	4.04E+06	0.27
1.50	0.0300	1.702	0.044	0.609	8.37E+05	10	6.40E+03	1.07E+04	5.69E+07	0.00
2.00	0.0001	2.300	0.011	0.662	8.60E+05	13	1.09E+04	1.73E+04	1.26E+07	0.88
2.00	0.0010	2.282	0.021	0.625	1.53E+06	14	8.20E+03	1.32E+04	1.37E+07	0.71
2.00	0.0020	2.262	0.026	0.618	1.90E+06	16	7.55E+03	1.35E+04	1.75E+07	0.67
2.00	0.0030	2.242	0.029	0.614	1.96E+06	16	7.35E+03	1.25E+04	3.02E+07	0.66
2.00	0.0040	2.222	0.032	0.613	2.00E+06	16	7.15E+03	1.19E+04	4.97E+07	0.65
2.00	0.0050	2.202	0.034	0.612	2.02E+06	17	6.96E+03	1.33E+04	2.00E+07	0.65
2.00	0.0100	2.102	0.042	0.610	1.79E+06	15	7.51E+03	1.18E+04	5.11E+07	0.62
2.00	0.0150	2.002	0.047	0.734	1.64E+06	16	9.18E+03	1.17E+04	6.65E+06	0.56
2.00	0.0200	1.902	0.052	0.624	1.42E+06	15	7.62E+03	1.24E+04	5.85E+07	0.47
2.00	0.0300	1.702	0.058	0.668	1.23E+06	15	7.62E+03	1.26E+04	4.50E+06	0.15
2.50	0.0001	2.300	0.013	0.754	4.47E+05	14	1.57E+04	2.28E+04	8.01E+07	1.17
2.50	0.0010	2.282	0.026	0.685	5.45E+05	11	1.26E+04	1.91E+04	1.87E+07	1.02
2.50	0.0020	2.262	0.032	0.655	8.11E+05	12	1.05E+04	1.51E+04	1.39E+07	0.91
2.50	0.0030	2.242	0.036	0.638	1.20E+06	14	9.37E+03	1.33E+04	1.76E+07	0.82
2.50	0.0040	2.222	0.040	0.627	1.66E+06	17	8.64E+03	1.34E+04	1.77E+07	0.77
2.50	0.0050	2.202	0.043	0.623	2.07E+06	20	8.22E+03	1.35E+04	8.86E+06	0.74
2.50	0.0100	2.102	0.052	0.630	2.54E+06	23	8.43E+03	1.28E+04	5.95E+07	0.70
2.50	0.0150	2.002	0.059	0.643	2.48E+06	23	7.98E+03	1.28E+04	5.75E+07	0.68
2.50	0.0200	1.902	0.064	0.660	2.17E+06	22	8.34E+03	1.27E+04	7.33E+06	0.63
2.50	0.0300	1.702	0.073	0.739	1.74E+06	22	8.36E+03	1.38E+04	6.03E+06	0.41
3.00	0.0001	2.300	0.016	0.840	2.28E+05	17	1.95E+04	2.76E+04	1.05E+08	332.70
3.00	0.0010	2.282	0.031	0.812	1.96E+05	13	1.85E+04	2.59E+04	1.09E+08	1.17
3.00	0.0020	2.262	0.039	0.777	2.61E+05	12	1.57E+04	1.81E+04	8.62E+07	1.11
3.00	0.0030	2.242	0.044	0.747	3.23E+05	11	1.53E+04	1.80E+04	7.46E+07	1.06
3.00	0.0040	2.222	0.048	0.722	4.10E+05	12	1.39E+04	1.69E+04	8.65E+07	1.03
3.00	0.0050	2.202	0.051	0.704	5.23E+05	12	1.28E+04	1.52E+04	8.45E+07	0.99
3.00	0.0100	2.102	0.063	0.659	1.16E+06	17	1.02E+04	1.33E+04	6.57E+07	0.83
3.00	0.0150	2.002	0.071	0.677	1.34E+06	18	9.79E+03	1.31E+04	1.00E+07	0.78
3.00	0.0200	1.902	0.077	0.719	1.33E+06	19	9.70E+03	1.35E+04	9.40E+06	0.74
3.00	0.0300	1.702	0.087	0.815	9.75E+05	18	9.78E+03	1.50E+04	7.95E+06	0.64
3.50	0.0001	2.300	0.018	0.876	1.76E+05	20	2.29E+04	3.40E+04	1.42E+08	548.33
3.50	0.0010	2.282	0.037	0.855	1.36E+05	15	2.33E+04	3.23E+04	1.11E+08	1.05
3.50	0.0020	2.262	0.045	0.842	1.42E+05	14	2.05E+04	2.77E+04	1.11E+08	1.09
3.50	0.0030	2.242	0.051	0.848	1.45E+05	12	1.91E+04	2.12E+04	5.00E+07	1.09

Continued on next page

(Table 3 continued)

$M_{initial}$	Z	α_{MLT}	η_B	M_{final}	τ_{TPAGB}	$\#TPs$	$L_{TP,avg}$	$L_{TP,max}$	$T_{bce,max}$	λ_{max}
3.50	0.0040	2.222	0.056	0.849	1.44E+05	11	1.86E+04	2.06E+04	4.30E+07	1.07
3.50	0.0050	2.202	0.060	0.853	1.46E+05	11	1.83E+04	2.06E+04	4.07E+07	1.07
3.50	0.0100	2.102	0.073	0.745	3.13E+05	12	1.41E+04	2.29E+04	7.38E+07	1.01
3.50	0.0150	2.002	0.083	0.780	4.49E+05	12	1.32E+04	1.57E+04	1.87E+07	0.95
3.50	0.0200	1.902	0.090	0.829	4.88E+05	13	1.27E+04	1.56E+04	1.61E+07	0.91
3.50	0.0300	1.702	0.102	0.967	3.86E+05	13	1.28E+04	1.88E+04	1.32E+07	0.80
4.00	0.0001	2.300	0.021	0.909	1.25E+05	20	2.71E+04	3.57E+04	1.28E+08	1139.93
4.00	0.0010	2.282	0.042	0.897	9.49E+04	16	2.47E+04	3.23E+04	1.13E+08	0.97
4.00	0.0020	2.262	0.052	0.885	9.71E+04	14	2.24E+04	2.84E+04	8.22E+07	0.97
4.00	0.0030	2.242	0.058	0.903	1.06E+05	14	2.16E+04	2.68E+04	7.28E+07	0.99
4.00	0.0040	2.222	0.064	0.907	1.11E+05	14	2.08E+04	2.57E+04	6.90E+07	0.99
4.00	0.0050	2.202	0.068	0.904	1.16E+05	13	2.05E+04	2.45E+04	6.57E+07	1.02
4.00	0.0100	2.102	0.084	0.923	1.21E+05	11	1.93E+04	2.16E+04	4.60E+07	1.01
4.00	0.0150	2.002	0.095	0.985	1.21E+05	11	2.04E+04	2.84E+04	3.70E+07	1.00
4.00	0.0200	1.902	0.103	0.921	1.04E+05	9	1.70E+04	2.60E+04	3.01E+07	0.97
4.00	0.0300	1.702	0.116	1.230	9.76E+04	8	1.74E+04	2.42E+04	2.42E+07	0.90
4.50	0.0001	2.300	0.024	1.090	8.53E+04	19	3.42E+04	4.34E+04	9.76E+07	1.04
4.50	0.0010	2.282	0.047	1.188	6.68E+04	16	3.42E+04	3.77E+04	9.32E+07	1.00
4.50	0.0020	2.262	0.058	0.938	7.14E+04	15	2.50E+04	3.38E+04	8.86E+07	0.96
4.50	0.0030	2.242	0.066	0.946	7.33E+04	14	2.43E+04	3.20E+04	8.58E+07	0.95
4.50	0.0040	2.222	0.072	0.951	7.75E+04	14	2.35E+04	3.02E+04	8.28E+07	0.97
4.50	0.0050	2.202	0.077	0.954	7.90E+04	13	2.29E+04	2.91E+04	8.05E+07	1.02
4.50	0.0100	2.102	0.094	0.983	8.82E+04	13	2.18E+04	2.67E+04	6.91E+07	0.98
4.50	0.0150	2.002	0.106	1.052	9.96E+04	13	2.10E+04	2.39E+04	5.75E+07	0.98
4.50	0.0200	1.902	0.116	1.076	8.63E+04	11	1.99E+04	2.59E+04	3.90E+07	0.96
4.50	0.0300	1.702	0.131	1.285	5.08E+04	7	1.91E+04	2.39E+04	2.99E+07	0.84
5.00	0.0001	2.300	0.026	0.975	6.08E+04	20	3.71E+04	5.36E+04	1.38E+08	1092.89
5.00	0.0010	2.282	0.052	0.962	4.64E+04	16	3.16E+04	4.59E+04	6.24E+08	1.07
5.00	0.0020	2.262	0.065	0.980	4.72E+04	14	2.79E+04	4.17E+04	9.65E+07	0.99
5.00	0.0030	2.242	0.073	0.992	4.97E+04	14	2.71E+04	3.87E+04	9.31E+07	0.98
5.00	0.0040	2.222	0.080	0.986	5.23E+04	13	2.60E+04	3.68E+04	9.08E+07	0.95
5.00	0.0050	2.202	0.085	0.988	5.97E+04	14	2.53E+04	3.47E+04	8.79E+07	0.94
5.00	0.0100	2.102	0.105	1.035	6.10E+04	13	2.42E+04	3.13E+04	8.00E+07	0.93
5.00	0.0150	2.002	0.118	1.106	6.87E+04	13	2.34E+04	2.93E+04	7.24E+07	0.94
5.00	0.0200	1.902	0.129	1.167	6.66E+04	12	2.22E+04	2.61E+04	6.32E+07	0.93
5.00	0.0300	1.702	0.146	1.505	6.05E+04	11	2.73E+04	3.30E+04	3.73E+07	0.87
6.00	0.0001	2.300	0.032	1.059	2.46E+04	19	5.45E+04	7.56E+04	5.63E+08	0.99
6.00	0.0010	2.282	0.063	1.054	1.44E+04	10	3.33E+04	6.47E+04	1.30E+08	0.77
6.00	0.0020	2.262	0.077	1.074	1.51E+04	9	3.25E+04	5.95E+04	1.06E+08	0.73
6.00	0.0030	2.242	0.088	1.078	1.72E+04	9	3.16E+04	5.52E+04	1.03E+08	0.76
6.00	0.0040	2.222	0.095	1.085	1.97E+04	10	3.10E+04	5.18E+04	1.00E+08	0.80
6.00	0.0050	2.202	0.102	1.088	2.17E+04	10	3.04E+04	4.95E+04	9.80E+07	0.83
6.00	0.0100	2.102	0.126	1.151	2.61E+04	11	2.92E+04	4.31E+04	9.16E+07	0.83
6.00	0.0150	2.002	0.142	1.190	2.64E+04	11	2.70E+04	3.98E+04	8.55E+07	0.78
6.00	0.0200	1.902	0.155	1.334	2.71E+04	11	2.67E+04	3.67E+04	7.88E+07	0.79
6.00	0.0300	1.702	0.175	1.054	1.98E+04	7	2.62E+04	4.29E+04	7.99E+07	0.67
7.00	0.0001	2.300	0.037	1.183	3.52E+03	9	5.92E+04	1.37E+05	5.88E+08	0.23
7.00	0.0010	2.282	0.073	1.367	2.07E+03	5	7.49E+04	1.22E+05	1.30E+08	0.02
7.00	0.0020	2.262	0.090	1.258	2.26E+03	4	5.33E+04	1.10E+05	1.26E+08	0.21
7.00	0.0030	2.242	0.102	1.275	2.60E+03	4	5.46E+04	1.02E+05	1.22E+08	0.23
7.00	0.0040	2.222	0.111	1.283	3.10E+03	5	3.97E+04	9.40E+04	1.14E+08	0.30
7.00	0.0050	2.202	0.119	1.283	3.62E+03	5	3.91E+04	8.87E+04	1.11E+08	0.33
7.00	0.0100	2.102	0.147	1.300	5.73E+03	6	3.38E+04	6.97E+04	1.01E+08	0.22
7.00	0.0150	2.002	0.165	1.387	8.79E+03	8	3.30E+04	5.99E+04	9.53E+07	0.51
7.00	0.0200	1.902	0.180	1.546	1.01E+04	9	3.21E+04	5.34E+04	8.90E+07	0.45
7.00	0.0300	1.702	0.204	1.142	7.84E+03	5	2.99E+04	6.28E+04	8.78E+07	0.20

Column Descriptions
Col 1: Initial mass of stellar model ($M_\odot$)
Col 2: Initial metal mass fraction
Col 3: Mixing length α, calculated as $\alpha_{MLT} = 2.3 - [20 \times (Z_i - 0.0001)]$
Col 4: Blöcker scaling factor η for mass loss on the AGB, calculated as $\eta_B = \frac{M_i}{12} \times Z_i^{0.3}$
Col 5: Final mass after last thermal pulse ($M_\odot$)
Col 6: Duration of thermally pulsing AGB phase (years)
Col 7: Number of thermal pulses experienced
Col 8: Average luminosity during thermal pulsing ($L_\odot$)
Col 9: Maximum luminosity during thermal pulsing ($L_\odot$)
Col 10: Maximum temperature at the base of the convective envelope during thermal pulsing (K)
Col 11: Maximum dredge-up efficiency, calculated as $\lambda = \Delta M_{dredged}$ / ΔM_{core}

REFERENCES

Abia, C. Cunha, K. Cristallo, S. de Laverny, P. 2015, A&A, 581, A88

Abia C., de Laverny P., Romero-Gómez M., Figueras F., 2022, A&A, 664, A45

Battino U., et al., 2019, Monthly Notices of the Royal Astronomical Society, 489, 1082

Battino U., Pignatari M., Tattersall A., Denissenkov P., Herwig F., 2022, Universe, 8

Blöcker T., 1995, A&A, 299, 755

Blöcker T., Herwig F., Driebe T., 2000, Mem. Soc. Astron. Italiana, 71, 711

Boothroyd A., Sackmann I., Wasserburg G., 1995, The Astrophysical Journal, 442

Bressan A., Fagotto F., Bertelli G., Chiosi C., 1993, A&AS, 100, 647

Bruzual G., Charlot S., 2003, MNRAS, 344, 1000

Campbell S. W., Lattanzio J. C., 2008, A&A, 490, 769

Canuto V. M., Mazzitelli I., 1991, ApJ, 370, 295

Charbonnel, C. Schaerer, D. Prantzos, N. Ramírez-Galeano, L. Fragos, T. Kuruvanthodi, A. Marques-Chaves, R. Gieles, M. 2023, A&A, 673, L7

Chiaki G., Wise J. H., Marassi S., Schneider R., Limongi M., Chieffi A., 2020, Monthly Notices of the Royal Astronomical Society, 497, 3149

Choi J., Dotter A., Conroy C., Cantiello M., Paxton B., Johnson B. D., 2016, ApJ, 823, 102

Colgan J., et al., 2016, The Astrophysical Journal, 817, 116

Cristallo S., Straniero O., Piersanti L., Gobrecht D., 2015, ApJS, 219, 40

Davies B., Kudritzki R.-P., Gazak Z., Plez B., Bergemann M., Evans C., Patrick L., 2015, ApJ, 806, 21

Farag E., et al., 2024, The Astrophysical Journal, 968, 56

Ferguson J. W., Alexander D. R., Allard F., Barman T., Bodnarik J. G., Hauschildt P. H., Heffner-Wong A., Tamanai A., 2005, The Astrophysical Journal, 623, 585

Finlator K., Doughty C., Cai Z., Díaz G., 2020, Monthly Notices of the Royal Astronomical Society, 493, 3223

Gavilán M., Buell, J. F. Mollá, M. 2005, A&A, 432, 861

Gehrz R. D., Allamandola L., Tielens A., 1989, in IAU symp. p. 445

Groenewegen M. A. T., Sloan G. C., 2018, A&A, 609, A114

Groenewegen M. A. T., Sloan G. C., Soszyński I., Petersen E. A., 2009, A&A, 506, 1277

Hansen T. T., Simon, J. D. Li, T. S. Frebel, A. Thompson, I. Shectman, S. 2023, A&A, 674, A180

Henyey L. G., Wilets L., Böhm K. H., Lelevier R., Levee R. D., 1959, ApJ, 129, 628

Herwig F., 2000, A&A, 360, 952

Herwig F., Austin S. M., 2004, The Astrophysical Journal, 613, L73

Höfner S., Olofsson H., 2018, A&ARv, 26, 1

Huscher E., Finlator K., Kušmić S., Steen M., 2024, The Astrophysical Journal, 966, 111

Jermyn A. S., et al., 2023, ApJS, 265, 15

Johnson J. W., Weinberg D. H., 2020, MNRAS, 498, 1364

Jorissen A., Smith V. V., Lambert D. L., 1992, A&A, 261, 164

Kalirai J. S., Saul Davis D., Richer H. B., Bergeron P., Catelan M., Hansen B. M. S., Rich R. M., 2009, ApJ, 705, 408

Karakas A. I., 2010, Monthly Notices of the Royal Astronomical Society, 403, 1413

Karakas A. I., Lattanzio J. C., 2014, Publ. Astron. Soc. Australia, 31, e030

Karakas A. I., Lugaro M., 2016, The Astrophysical Journal, 825, 26

Karakas A. I., Lugaro M., Carlos M., Cseh B., Kamath D., García-Hernández D. A., 2018, Monthly Notices of the Royal Astronomical Society, 477, 421

Karakas A. I., Cinquegrana G., Joyce M., 2022, MNRAS, 509, 4430

Kippenhahn R., Weigert A., Weiss A., 2012, Mass Loss. Springer Berlin Heidelberg, Berlin, Heidelberg, pp 83–85, doi:10.1007/978-3-642-30304-3_9, `https://doi.org/10.1007/978-3-642-30304-3_9`

Li Q., Narayanan D., Davé R., 2019, Monthly Notices of the Royal Astronomical Society, 490, 1425

Lucatello S., Masseron T., Johnson J. A., Pignatari M., Herwig F., 2011, ApJ, 729, 40

Lugaro M., Ugalde C., Karakas A. I., Görres J., Wiescher M., Lattanzio J. C., Cannon R. C., 2004, ApJ, 615, 934

Magg E., et al., 2022, A&A, 661, A140

Magic Z., Weiss A., Asplund M., 2015, A&A, 573, A89

Marigo P., 2001, A&A, 370, 194

Marigo P., et al., 2020, Nature Astronomy, 4, 1102

Mattsson L., Wahlin R., Höfner S., Eriksson K., 2008, A&A, 484, L5

Nakajima K., Ouchi M., Isobe Y., Harikane Y., Zhang Y., Ono Y., Umeda H., Oguri M., 2023, The Astrophysical Journal Supplement Series, 269, 33

Oppenheimer B. D., Davé R., 2008, Monthly Notices of the Royal Astronomical Society, 387, 577

Osborn Z., Karakas A. I., Kemp A. J., Izzard R., Kamath D., Lugaro M., 2024, arXiv e-prints, p. arXiv:2412.01025

Paxton B., Bildsten L., Dotter A., Herwig F., Lesaffre P., Timmes F., 2011, ApJS, 192, 3

Paxton B., et al., 2013, ApJS, 208, 4

Paxton B., et al., 2015, ApJS, 220, 15

Paxton B., et al., 2018, ApJS, 234, 34

Paxton B., et al., 2019, ApJS, 243, 10

Rahmati A., Schaye J., Crain R. A., Oppenheimer B. D., Schaller M., Theuns T., 2016, MNRAS, 459, 310

Rees N. R., Izzard R. G., Karakas A. I., 2024, MNRAS, 527, 9643

Reimers D., 1975, Mem. Soc. R. Sci. Liege, v. 8, pp. 369-382

Sackmann I. J., Boothroyd A. I., 1992, ApJ, 392, L71

Straniero O., Gallino R., Cristallo S., 2006, Nuclear Physics A, 777, 311–339

Straniero O., Abia C., Domínguez I., 2023, The European Physical Journal A, 59, 17

Tayar J., et al., 2017, ApJ, 840, 17

Tinsley B. M., 1980, Fundamentals Cosmic Phys., 5, 287

Trampedach R., Stein R. F., Christensen-Dalsgaard J., Nordlund Å., Asplund M., 2014, MNRAS, 442, 805

VandenBerg D. A., Swenson F. J., Rogers F. J., Iglesias C. A., Alexander D. R., 2000, ApJ, 532, 430

Vassiliadis E., Wood P. R., 1993, ApJ, 413, 641

Ventura P., D'Antona F., 2005, A&A, 431, 279

Ventura P., Marigo P., 2010, Monthly Notices of the Royal Astronomical Society, 408, 2476

Ventura P., Karakas A. I., Dell'Agli F., García–Hernández D. A., Boyer M. L., Di Criscienzo M., 2016, Monthly Notices of the Royal Astronomical Society, 457, 1456

Ventura P., Karakas A., Dell'Agli F., García–Hernández D. A., Guzman-Ramirez L., 2018, Monthly Notices of the Royal Astronomical Society, 475, 2282

Vitense E., 1953, Z. Astrophys., 32, 135

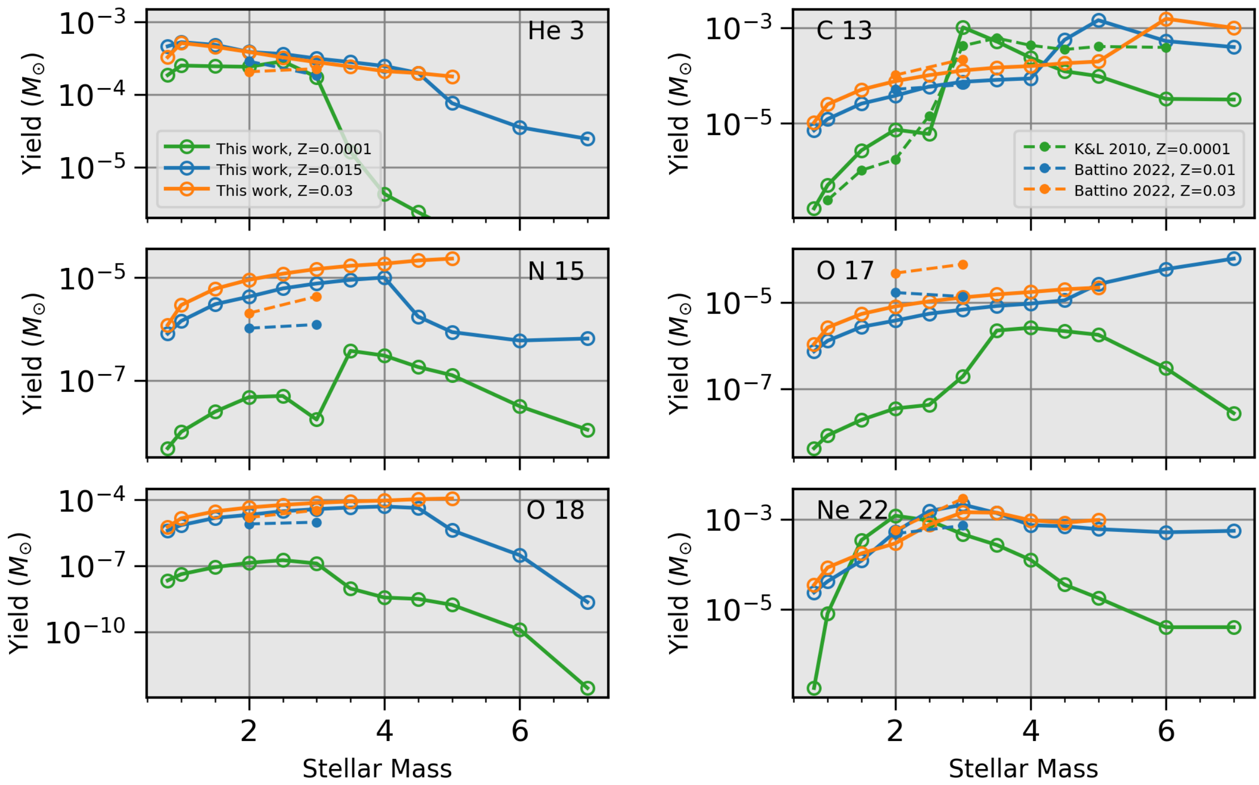

Figure A1. More ejected isotope yields as a function of initial stellar mass for 3 initial metallicities: nearly metal free (0.0001), solar (0.015), and supersolar (0.03). For comparison, yields from Karakas 2010 (C13 at Z=0.0001) and Battino et al. 2022 (Z=0.01 and Z=0.03 at 2M$_\odot$ and 3M$_\odot$) are included.

APPENDIX A: YIELDS OF ADDITIONAL ISOTOPES

APPENDIX B: OBSTACLES AND CONSIDERATIONS FOR AGB MODELING

Models with higher initial metallicity are more challenging to numerically solve than those with lower metallicity. These stars can be more complex due to higher opacities, more rapid mass loss, and the intricate interplay of physical processes during the thermal pulsing phase

The scaling of the mass loss parameter as a function of metallicity employed in this paper helped the problem, but did not solve it completely. High-mass (>3.5M) models with Z=0.02 and especially with Z=0.03 consistently saw a very small dt per timestep, effectively bring progress to zero. To achieve the desired final stellar mass and average luminosity to match observations (see Figure 2), it became necessary to increase the mass loss scaling factor slightly:

$$\eta = \frac{M}{10M_\odot} \times Z^{0.3} \tag{B1}$$

Another obstacle one may encounter involves models of higher initial metallicity. It is common to use the composition of the core as an indicator to transition between different stellar phases. For example, we initially set a central helium mass fraction of 0.985 to denote the transition from the Red Giant Branch (RGB) to the Horizontal Branch, but while this value works well for most models, it proved too high for supersolar metallicity models. These models at this stage had larger central fractions of nitrogen, oxygen, and neon at this point so manually lowering the threshold becomes required to complete the RGB and progress in the star's evolution.